Taylor & Francis
Taylor & Francis Group

International Journal of Remote Sensing

ISSN: (Print) (Online) Journal homepage: https://www.tandfonline.com/loi/tres20

SAAC-Net: deep neural network-based model for atmospheric correction in remote sensing

Maitrik Shah, Mehul S Raval, Srikrishnan Divakaran, Debajyoti Dhar & Hasit Parmar

To cite this article: Maitrik Shah, Mehul S Raval, Srikrishnan Divakaran, Debajyoti Dhar & Hasit Parmar (2023) SAAC-Net: deep neural network-based model for atmospheric correction in remote sensing, International Journal of Remote Sensing, 44:23, 7365-7389, DOI: 10.1080/01431161.2023.2282407

To link to this article: https://doi.org/10.1080/01431161.2023.2282407

Published online: 30 Nov 2023.

INTERNATIONAL JOURNAL OF REMOTE SENSING
2023, VOL. 44, NO. 23, 7365–7389
https://doi.org/10.1080/01431161.2023.2282407

SAAC-Net: deep neural network-based model for atmospheric correction in remote sensing

Maitrik Shah [a], Mehul S Raval [a], Srikrishnan Divakaran [b], Debajyoti Dhar [c] and Hasit Parmar [d]

[a]School of Engineering and Applied Science, Ahmedabad University, Ahmedabad, India; [b]School of Interwoven Arts and Sciences, Krea University, Sricity, India; [c]Signal and Image Processing Group, Space Application Centre (SAC), Indian Space Research Organisation (ISRO), Ahmedabad, India; [d]Computer Engineering department, L. D. College of Engineering, Ahmedabad, India

ABSTRACT

Atmospheric correction eliminates corruption in reflectance captured by satellite images due to atmospheric elements like gases, aerosols, and water vapours. Existing physics-based approaches employ radiative transfer models constructed using lookup tables computed for different atmospheric parameters. However, these approaches are computationally expensive and rely on estimates of parameters that are difficult to sense accurately. This paper proposes a deep learning model as an alternative to physics-based approaches. We present an end-to-end deep neural network trained on seasonally and spatially rich Landsat 8 satellite images without explicit atmospheric parameterization along with our analysis and its validation. We validate the model's effectiveness vis-a-vis Landsat 8's Land Surface Reflectance Code – LaSRC results in $RMSE\sim0.042$, $SSIM\sim0.97$, and correlation coefficient $r\sim0.99$. For ground measurements by RadCalNet, the proposed model has an $RMSE\sim0.053$, $SSIM\sim0.90$, and $r\sim0.88$. The results show that the model accurately predicts surface reflectance and correlates highly with reference data.

ARTICLE HISTORY
Received 20 May 2023
Accepted 26 October 2023

KEYWORDS
Atmospheric correction; deep learning; satellite images; surface reflectance; top of the atmosphere

1. Introduction

For many geospatial applications, satellites exploit the physical and chemical compositions of the observed surface through its surface reflectance (SR) while estimating vegetation indices, leaf area index, and other biophysical parameters. SR is defined as the fraction of incoming sunlight that the surface reflects, known as the bottom of atmosphere (BOA) reflectance. It differs from the top-of-atmosphere (TOA) reflectance sensed by satellite sensors due to solar illumination and effects from atmospheric elements like gases, aerosols, and water vapour. Hence, the sensed reflectance value, i.e. TOA, differs from BOA. Atmospheric correction (AC) must be carried out to estimate SR to factor in the effect of atmospheric elements. Many remote sensing applications, such as burned area identification (Zhang et al. 2015), water depth estimation (Saeidi et al. 2023), CO_2 estimation for

CONTACT Mehul S Raval mehul.raval@ahduni.edu.in School of Engineering and Applied Science, Ahmedabad University, Commerce Six Roads, Navrangpura, Ahmedabad 380009, India

carbon neutrality (Chen 2021), soil organic carbon (Angelopoulou et al. 2019), require accurate estimation of SR, which shows the importance of AC for quantitative remote sensing. AC is highly challenging because of its dependence on estimates of solar illumination and distortion due to gases, aerosols, and water vapour that are not measurable at acquisition time. AC has led to many approaches, from traditional, accurate, and reliable physics-based approaches to simple image-based approaches.

Physics-based approaches in remote sensing depend on analytical models of radiative transfer that incorporate atmospheric parameters like aerosol optical depth (AOD) and column water vapour (CWV), along with geometric parameters such as solar zenith angle, solar azimuth angle, and relative azimuth angle. These parameters play a crucial role in accounting for the complex interactions involving the absorption and scattering of electromagnetic radiation. While geometric parameters are readily obtainable, obtaining atmospheric parameters presents a challenge. Typically, physics-based methods involve estimating these atmospheric parameters of the Radiative Transfer Models (RTMs) and subsequently utilizing them to compute SR using pre-computed Lookup Tables (LUTs) that are defined in terms of these estimated atmospheric parameters. Figure 1(a) illustrates a block diagram of the physics-based atmospheric correction approach. Fast Line-of -sight Atmospheric Analysis of Spectral Hypercubes (FLAASH) (Anderson et al. 2002), Atmospheric and Topographic Correction (ATCOR) (Richter and Schläpfer 2019), 6S (Second Simulation of the Satellite Signal in the Solar Spectrum) (Kotchenova and Vermote 2007; Vermote et al. 1997), and Land Surface Reflectance Code (LaSRC) (Vermote et al. 2016) are some of the Physics-based models. FLAASH is an AC model based on MODerate resolution atmospheric TRANsmission (MODTRAN-4) that eliminates the scattering and absorption effect caused by atmospheric molecules by estimating atmospheric parameters from atmospheric characteristics in image pixels. ATCOR and its variants ATCOR-2, ATCOR-3, and ATCOR-4, also based on MODTRAN-4, mainly utilized for airborne remotely sensed images, perform AC by first removing the effect of the

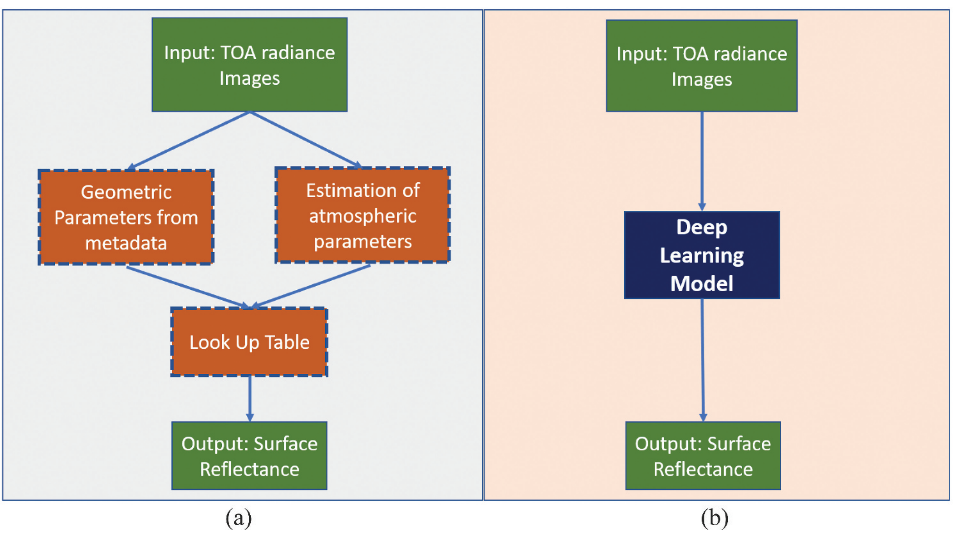

Figure 1. Block diagram of (a) AC using physics-based models and (b) AC using deep learning models.

atmosphere by ignoring the adjacency effect and then account for radiance from the neighbourhood. 6SV is the vector version of 6S designed to predict the reflectance at the TOA, simulating the various atmospheric conditions. It is mainly used to construct LUTs in the AC algorithm and is based on the method of successive orders of scattering approximations. LaSRC was designed explicitly for AC of Landsat-8 images but is now used in Sentinel-2 and other sensors. Based on the 6S RTM, it carries the heritage of the previous LEDAPS algorithms implemented for Landsat-5 and Landsat-7.

Physics-based AC methods for remote sensing, while known for their precision, come with inherent complexities. The construction of LUTs involves extensive simulations of diverse atmospheric conditions with distinct atmospheric profiles. Subsequent interpolation and estimation during the AC process introduce potential biases and variability into the SR estimation process. Moreover, these models require a deeper understanding of physics and are challenging to interpret, extend, and generalize. The accuracy and assumptions of the physical equations limit their performance. Also, due to large-scale atmospheric changes, the extrapolation of a physics-based model is complex as it requires significant re-tuning for new conditions. Furthermore, they rely on atmospheric parameters that require intricate modelling, involve approximations, and demand significant computational resources. Atmospheric parameters, like aerosol optical depth and column water vapour, are estimated through parametric simulations by analysing specific image regions or utilizing a reference target with known spectral properties in the monitored scene.

Several AOD retrieval algorithms, such as Dark Target (Jackson et al. 2013; Kaufman et al. 1997), Deep Blue (Hsu et al. 2006), and Multi-Angle Implementation of Atmospheric Correction (Lyapustin et al. 2012), have been developed and commonly use RTMs to determine AOD from TOA data. However, there is a notable level of uncertainty in AOD retrieval due to the challenge of accurately parameterizing fundamental aerosol optical properties. This challenge is particularly pronounced in regions with complex terrain and arid or semi-arid environments. Similarly, there are various approaches for estimating CWV, with techniques like Atmospheric Pre-corrected Differential Absorption (Schläpfer et al. 1998) and Low-Rank Subspace Projection-Based Water Estimator (Acito and Diani 2018) being commonly used. However, these algorithms have limitations, such as reliance on unrealistic physical assumptions or dependence on other difficult-to-obtain parameters. AOD and CWV are crucial parameters for SR estimation from TOA data, and any errors in estimating these parameters introduce uncertainty in the SR derivation. Therefore, precise estimation of these parameters is of utmost importance.

In recent developments, a few approaches have used Deep Learning (DL) models to estimate these parameters. It is vital to note that AOD is a critical parameter in AC Zhou et al. (2023) due to its complex relationship with TOA. Authors in (She et al. 2020) and She et al. (2022) have explored DL models to learn this complex relationship and have estimated AOD values. DL-generated values are then compared with values provided by the AERONET site (Holben et al. 1998), which calculates AOD values using a traditional approach. The authors concluded that the DL model was as accurate as the physics-based RTM. In similar attempts, DIOUF, Niang, and Thiria (2019) and Acito, Diani, and Corsini (2020) used DL models to estimate CWV. The DL model in Acito, Diani, and Corsini (2020) estimates CWV values using only the flight height. It does not use solar zenith angle and atmospheric visibility, which are vital parameters for traditional CWV estimation methods. Despite these approaches utilizing

DL models to estimate various atmospheric parameters, there remains a reliance on physics-based RTMs for retrieving SR values from TOA imagery.

On the other hand, image-based approaches perform AC using only remotely sensed images captured by satellite or airborne sensors without requiring any atmospheric parameters as input; instead, they only use the information in the image itself. The simplest image-based method is the Dark Object Subtraction (Chavez 1988). It performs AC by finding the darkest pixels in the image and subtracting their values from all pixels. It works on the assumption that the few objects on the earth are in complete shade, so their reflectance values should be zero. Non-zero reflectance values of these objects are due to atmospheric scattering. The empirical line method (Smith and Milton 1999) forces image spectral data to match the target object's reflectance spectra. At least two low and high reflectance targets must be identified from the scene. Another image-based AC is a Quick Atmospheric Correction (QuAC) (Smith and Milton 2012) is a model, which works on the assumption that the mean spectrum of a collection of diverse material spectra is invariant from scene to scene. QuAC works well if at least 10 different objects are contained in the background. Image-based approaches are simple and computationally efficient, but their accuracy in seasonal and spectral variability situations limits these approaches from quickly obtaining a first-order approximation of SR values.

This motivated us to explore DL models to obtain accuracy that is comparable to physics-based methods while retaining computational efficiency. Moreover, DL models do away with the requirements of requiring any atmospheric parameters and geometric parameters as input. DL models offer several advantages: they automatically learn features, simplifying model building and training; they are computationally efficient compared to physics-based models (Yao et al. 2023). With their ability to capture complex nonlinear relationships between input and target variables, DL models are highly adaptable to changing atmospheric conditions and sensor characteristics. DL enables the development of models with increasingly higher semantic layers and complexity through iterative learning processes, offering both accuracy and computational efficiency. DL's potential has been demonstrated in various applications within remote sensing imagery, encompassing tasks such as change detection, segmentation, and classification (Fadaeddini, Eshghi, and Majidi 2018; Zhao et al. 2021; Peng, Zhang, and Guan 2019). Techniques like stacked autoencoders, convolutional neural networks (CNNs), and vision transformers are harnessed for spectral-spatial and temporal feature extraction (Tarasiou, Chavez, and Zafeiriou 2023; Gao, Chen, and Feng 2022; Chen et al. 2016). Additionally, DL models are increasingly applied in numerical weather prediction (Manil et al. 2020) and radiative transfer modelling (Liu and Liang 2023).

Here, we propose an innovative DL-based approach for atmospheric correction in remote sensing imagery, eliminating the reliance on atmospheric parameters, geometric parameters, and LUTs and instead focusing solely on input images as shown in Figure 1(b). To our knowledge, no prior work has been published applying DL techniques to AC, opening up promising avenues in this domain. The DL model we have designed, named Season Aware Atmospheric Correction Network (SAAC-Net), is an end-to-end DL model and is trained with a spatially and seasonally rich dataset spanning diverse land covers (LCs) and seasons, enhancing its generalization and

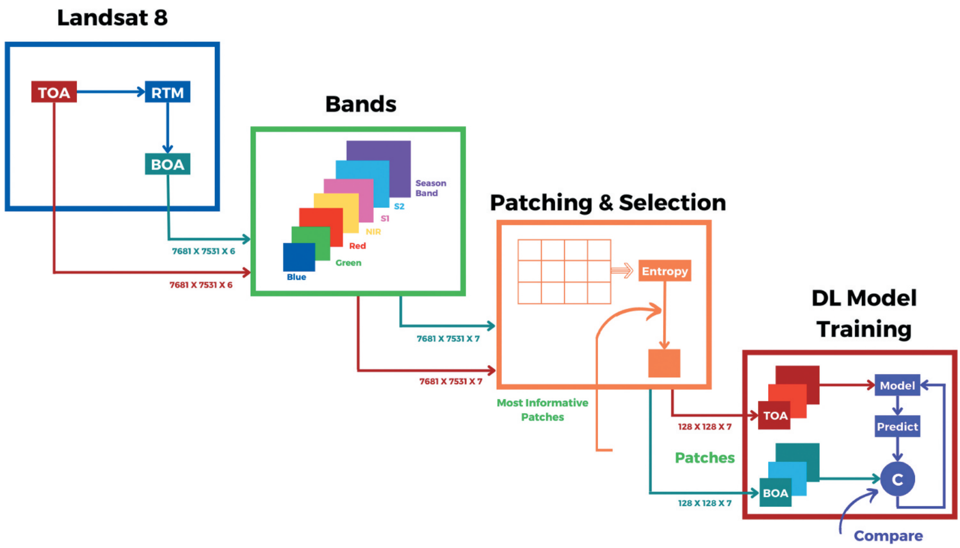

Figure 2. Block diagram of the proposed approach.

performance. This is crucial as the reflectance of LC is subject to change with seasons due to variations in AOD (Acharya and Sreekesh 2013) and CWV (Patel and Kuttippurath 2022). SAAC-Net uses a CNN with residual blocks (RBs) with global and local skip connections to address the vanishing gradient problem challenge and foster improved training and learning capabilities.

The paper is organized as follows: A detailed discussion about the proposed approach containing dataset details and model architecture is covered in Section 2. Section 3 is dedicated to the SAAC-Net performance evaluation, extensive analysis, and discussions. Section 4 is dedicated to sensitivity analysis covering seasons, skip connections, residual blocks, and dataset size. Finally, Section 5 concludes the paper and discusses the future extension of this research.

2. Proposed approach

A block diagram of the proposed approach is shown in Figure 2. The TOA and BOA image pairs are obtained from the Landsat 8 OLI sensor. A synthetic seasonal band is introduced as the seventh band in the image data to augment the model's understanding of seasonal variations. During the summer season, this band assumes a uniform value of 1 across all pixel locations, while during winter, it uniformly registers a value of 0. The subsequent step involves partitioning these images into patches, each measuring 128 $\times$ 128 pixels. These selected patches are then forwarded to the DL model for training.

Experiments have been conducted using Landsat 8 satellite data and Radiometric Calibration Network (RadCalNet) data to show the effectiveness of the proposed model details of which are provided in the next section.

2.1. Dataset details

SAAC-Net is trained and tested using Landsat 8 satellite data, providing multispectral imagery of the Earth's surface. It provides TOA and BOA image pairs, making it a suitable dataset for training and testing the SAAC-Net. The model's performance is also evaluated with ground observations provided by the RadCalNet. This section discusses the Landsat 8 dataset (Roy et al. 2014) and the RadCalNet dataset (Bouvet et al. 2019).

2.1.1. Landsat 8 satellite data

Landsat 8 Operational Land Imager (OLI) provides both TOA and BOA image pairs with 30 m spatial resolution and 16 days temporal resolution. We have used the following bands in the study: Blue ($0.45\mu m - 0.51\mu m$), Green ($0.53\mu m - 0.59\mu m$), Red ($0.64\mu m - 0.67\mu m$), Near-Infra-Red (NIR: $0.85\mu m - 0.88\mu m$), Short-Wave-IR-1 (SWIR1: $1.57\mu m - 1.65\mu m$), and SWIR2 ($2.11\mu m - 2.29\mu m$). Landsat 8 uses the LaSRC (Vermote et al. 2016) physics-based atmospheric correction algorithm to generate a BOA from a TOA. The training dataset uses different land covers to generalize SAAC-Net for spatial variations and different seasons to accommodate seasonal variations.

SAAC-Net is trained using a dataset comprising six Land Cover (LC) types from the International Geosphere-Biosphere Programme – IGBP global vegetation classification scheme, covering approximately 80% of India's landmass, to provide spatial variability and generalization capabilities. This diverse dataset includes Urban Land, Crop Land, Deciduous Forest, Evergreen Forest, Fallow Land, and Waste Land, ensuring the model can adapt to different spectral signatures from various LC types. Additionally, including varied terrains accounts for significant variations in aerosol optical depth and column water vapour across India, enabling the model to generalize effectively.

India experiences four distinct seasons: Winter (December–March), Summer (April–June), Monsoon (June–September), and Post-Monsoon (October–December) (Division 2020). These seasonal variations significantly influence atmospheric conditions, vegetation growth, and land surface characteristics, consequently top-of-atmosphere reflectance values. In our study, we have focused on the extreme seasons of India, namely summer and winter, as they exhibit a substantial contrast in reflectance values. For instance, the mean TOA reflectance difference between summer and winter across all land covers is 0.04. To ensure data quality, we selected images with a cloud cover of less than 15% for this study. Notably, the rainy season has been excluded from our analysis due to the prevalence of extensive cloud cover during this period in India.

The specific LC and details of the training and testing dataset are given in Tables 1 and 2, respectively. Representative images from both the training and testing datasets are visually depicted in Figure 3. Twenty-one images of the summer and twenty-five of the winter season of 2019 and 2020 from six locations have been used to train the model. The size of each Landsat 8 image is 7681×7531 pixels. We perform patch-based image processing and divide each image into small, non-overlapping patches. Four hundred most informative patches of size 128×128 pixels using information entropy have been chosen from each image. Hence, our training dataset contains 18,400 patches of size 128×128 pixels, out of which 80% are used for training and 20% for validation. The trained model takes only 0.10 seconds to perform AC for the patch of size 128×128 pixels.

Table 1. LC type and location for the Landsat 8 training dataset. All images are of months March, April, and May (Summer season) and November, December, and January (Winter season) of years 2019 and 2020. Image size: 128×128 pixels. 3200 images per LC, except 2400 for Evergreen Forest.

Seq. No.	Land-cover Types	Location	Lat-Lon	Landsat Rowpath	Summer	Winter
1	Urban Land	Kolkata, West Bengal	22.57°N, 88.36°E	138044	20.04.2019, 06.05.2019, 06.04.2020, 08.05.2020	30.01.2019, 30.11.2019, 01.01.2020, 02.12.2020
2	Crop Land	Hansi, Haryana	29.05°N, 76.08°E	147040	03.04.2019, 05.05.2019, 04.03.2020, 07.05.2020	29.01.2019, 29.11.2019, 30.10.2020, 01.12.2020
3	Deciduous Forest	Sukma, Chhattisgadh	21.28°N, 81.87°E	142045	31.03.2019, 18.05.2019, 02.04.2019, 04.05.2019	10.01.2019, 11.02.2019, 28.12.2019, 13.01.2020
4	Evergreen Forest	Arunachal West, Arunachal Pradesh	28.22°N, 94.73°E	135041	14.03.2019	25.01.2019, 25.11.2019, 28.01.2020, 19.12.2020, 11.11.2020
5	Fallow Land	Churu, Rajasthan	28.29°N, 74.97°E	148040	26.04.2019, 28.05.2019, 12.04.2020, 14.05.2020	04.11.2019, 23.01.2020, 08.12.2020, 24.12.2020
6	Waste Land	Jaisalmer, Rajasthan	26.92°N, 70.91°E	150041	24.04.2019, 10.05.2019, 26.04.2020, 12.05.2020	02.01.2019, 03.02.2019, 04.12.2019, 21.01.2020

Table 2. LC type and location for the Landsat 8 testing dataset. All images are of months March, April, and May (Summer season) and November, December, and January (Winter season) of years 2019 and 2020. Image size: 128×128 pixels. 800 images per LC.

Seq. No.	Land Cover Types	Location	Lat-Lon	Landsat Rowpath	Summer	Winter
1	Urban Land	Ahmedabad, Gujarat	23.02°N 72.57°E	148044	14.05.2020	24.12.2020
2	Crop Land	Jalandhar, Punjab	30.90°N 75.85°E	148039	28.05.2019	08.12.2020
3	Deciduous Forest	Tuithiang, Mizoram	23.73°N 92.72°E	135044	01.04.2020	29.12.2020
4	Evergreen Forest	Tamenglong, Manipur	24.59°N 93.39°E	135043	01.04.2020	27.11.2020
5	Fallow Land	Bikaner, Rajasthan	28.00°N 73.30°E	149041	05.05.2020	29.11.2020
6	Waste Land	Kutch, Gujarat	24.07°N 69.52°E	150043	26.05.2019	20.11.2020

For testing, a similar representative dataset with spatial and seasonal variability has been constructed to analyse the performance of the proposed network. It is to be noted that the geographical locations representing each LC in the test dataset are different from the training set. A total of 4800 non-overlapped patches (800 for each location) were used to test the model.

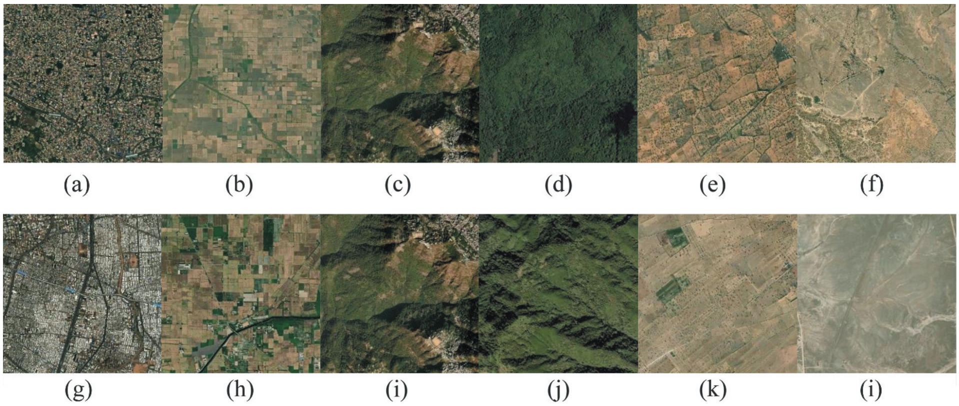

Figure 3. The first row shows the training images (a - f), and the second row shows testing images (g - l) for the following LC in order from left to right - Urban land, cropland, Deciduous Forest, Evergreen Forest, Fallow land, and wasteland.

Table 3. RadCalNet data characteristics.

Site	Land Cover	ROI	Latitude-Longitude	No. of Datapoints
RailRoad - U.S.A.	Waste Land	1km×1km	38.49°N,-115.69°E	15
La Crau - France	Crop Land (Sparse Vegetation)	90m×90m	43.55°N, 4.86°E	15
Gobabeb - Namibia	Waste Land	90m×90m	−23.60°N, 15.110°E	15

2.1.2. RadCalNet data

RadCalNet (Bouvet et al. 2019) is an initiative of the working group on calibration and validation of the committee on earth observation satellites. It has automated ground instruments to provide continuous SR measurements and other atmospheric parameters to derive TOA for different RadCalNet sites. All measurements are acquired every 30 min between 09:00 and 15:00 h local time, in the spectral range from 380 nm to 2500 nm with 10 nm spectral resolution.

We chose three locations for the study as described in Table 3. For each site, we collected 15 data points for 2019–2021. We also ensured that the data of the Landsat 8 image and RadCalNet data were the same. Based on the spatial resolution of the Landsat 8 OLI (30 m) and the representative region of RadCalNet with 30×30 pixels, this translated to 1 km×1 km region of interest (ROI) for RailRoad and a 3×3 pixel resulted into a 90 m×90 m ROI for La Crau and Gobabeb. The ROIs centred around the latitude/longitude of each region are shown in Table 3. By incorporating RadCalNet data into the experiments, the proposed model is rigorously tested and validated against SR captured using an on-site spectrometer, enhancing the credibility of the results.

2.2. SAAC-Net architecture

The proposed SAAC-Net, shown in Figure 4, is built upon a CNN structure incorporating cascaded RBs with global and local skip connections. This design choice brings several advantages to the model's performance. Cascaded RBs enhance gradient flow, allowing

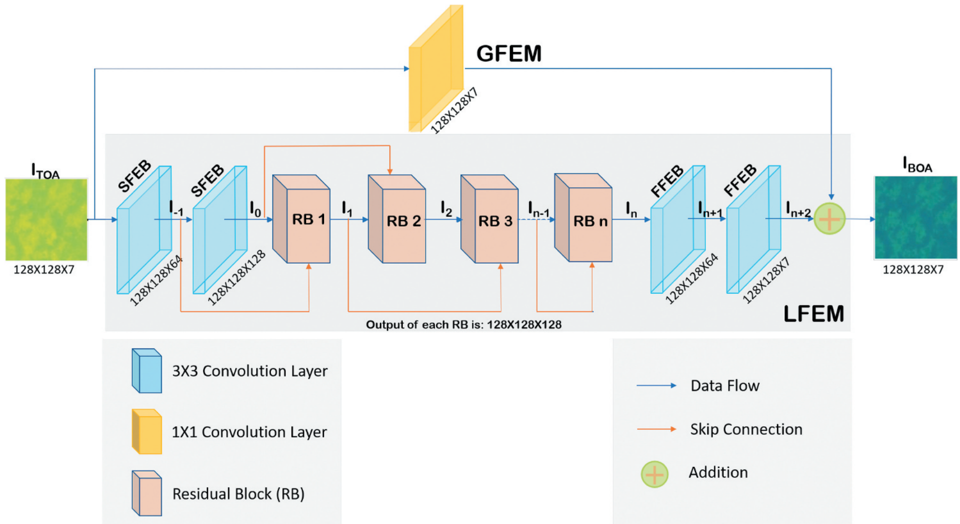

Figure 4. The proposed SAAC-Net architecture for AC with LFEM and GFEM.

initial layers to learn quickly, and residual connections facilitate the training of deeper networks. They also boost the network's representational capacity, enabling learning intricate hierarchical features. Additionally, skip connections provide implicit regularization, prevent overfitting, and efficiently train different network parts by skipping non-useful layers, preserving gradient information, and enhancing accuracy.

SAAC-Net establishes a comprehensive learning mechanism by incorporating local and global skip connections. The architecture encompasses two distinct modules: the Local Residual Feature Extraction Module (LFEM) and the Global Feature Extraction Module (GFEM). This mechanism allows the model to extract and utilize information at various scales effectively. Including local skip connections ensures that information is efficiently exchanged between neighbouring layers within the network. It aids in the model's ability to capture fine-grained details and subtle features in the data. On the other hand, the global skip connections allow for the integration of information from input to output of the network, enabling SAAC-Net to understand and exploit coarse-grained features across the entire dataset.

LFEM comprises shallow feature extraction blocks (F_{SFEB}), cascaded RBs, and final feature extraction blocks (F_{FFEB}). The F_{SFEB} consists of two 3×3 convolution blocks with 64 and 128 filters to extract the shallow features of the TOA image, which are then fed into the cascaded RBs.

$$I_{-1} = F_{SFEB-64}(I_{TOA}) \tag{1}$$

$$I_0 = F_{SFEB-128}(I_{-1}) \tag{2}$$

The internal architecture of the RB is a variant of the block reported in (Kaiming et al. 2016) and shown in Figure 5. Each RB consists of two 3×3 convolution blocks with 128 filters and ReLU activation units. Throughout the model, we use 3×3 convolution kernels since deeper networks with small kernel size work well (Simonyan, Zisserman, and Zisserman

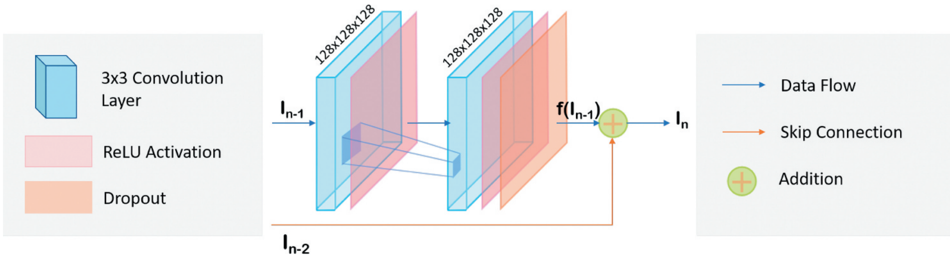

Figure 5. Residual blocks used in the SAAC-Net.

2014). Dropout (30%) is introduced after the second convolution block to regularize the training of SAAC-Net. $f(I_{n-1})$ is the output after this dropout layer, which represents the features extracted from layer I_{n-1}. Finally, a fusion of $f(I_{n-1})$ and I_{n-2} is added to produce an output of an RB.

$$I_n = f(I_{n-1}) + I_{n-2} \tag{3}$$

The last residual block's output is passed through the final feature extraction block (FFEB). F_{FFEB} consists of two 3×3 convolution blocks with 64 and 7 filters to maintain the channel dimension of the output image.

$$I_{n+1} = F_{FFEB-64}(I_n) \tag{4}$$

$$I_{TOA,LF} = F_{FFEB-7}(I_{n+1}) \tag{5}$$

$I_{TOA,LF}$ represents the fine-grained features of the input TOA image generated by the LFEM, and it learns the non-linear spectral mapping between TOA and SR values. However, it loses spatial information due to many convolutions.

The GFEM module inputs the I_{TOA} image. It applies the 1×1 convolution filters, extracting the coarse-grained features from the image and helping to preserve the spatial characteristics of the input image at the output (Litu et al. 2019).

$$I_{TOA,GF} = F_{GFEB-7}(I_{TOA}) \tag{6}$$

GFEB is the Global feature Extraction Block, which uses a 1×1 convolution filter, and $I_{TOA,GF}$ represents the coarse features of the input TOA image generated by the GFEM. It maintains the spatial resolution of the original image, and its coarse-grained features complement the LFEM features. Finally, fusion generates the BOA image by adding the coarse and fine features.

$$I_{BOA} = I_{TOA,LF} + I_{TOA,GF} \tag{7}$$

3. Results and discussion

This section presents comprehensive information pertaining to the experimental configuration, assessment metrics, and outcomes from the evaluation conducted on Landsat 8 test data across different LCs and geographic regions. Results of the evaluation with

RadCalNet data and a comparison with other models are also provided. We also interpret and discuss results in the same section to enhance the flow and coherence of the paper.

3.1. Experimental setup

All experiments have been conducted on a workstation with a 16GB GPU equipped with an x86-based Intel processor that uses NVIDIA Pascal architecture (P5000/6000). After doing an empirical experiment with patch sizes of (128×128, 256×256) and learning rates (0.01, 0.001, 0.0001), we selected a patch size of 128×128 as it provides balanced spatial coverage with moderate computational complexity. This is substantiated by the consideration that increasing the patch size would increase the number of parameters quadratically, subsequently augmenting the memory requirements. Moreover, it is noteworthy that the 128×128 patch size effectively spans an area encompassing approximately 3.8 km×3.8 km, sufficient to capture spectral variations. We use a 0.001 learning rate throughout the training, L2 loss function, and ADAM optimizer with β_1 (exponential decay rate for the first moment estimates) = 0.9 and β_2 (exponential decay rate for the second-moment estimates) = 0.999 values for faster convergence and better stability. The entire code has been implemented in Python with Keras and TensorFlow open-source libraries.

3.2. Evaluation metrics

Statistical analyses were performed to evaluate the performance of SAAC-Net. We compute the root mean square error (RMSE) to determine the statistical deviation of SAAC-Net predicted SR values from Landsat 8 LaSRC SR values, as shown in Equations 8. It quantifies accuracy, is easy to interpret, can compare methods, and suggests improvements.

$$RMSE = \sqrt{\frac{\sum_{i=1}^{n_\lambda} \left(\Delta\rho_{i,\lambda}\right)^2}{n_\lambda}} \tag{8}$$

where, n_λ is the number of pixels in band λ. $\rho_{i,\lambda}$ is the reflectance value in the band λ and pixel i, $\Delta\rho_{i,\lambda}$ is the difference of SAAC-Net predicted SR values and Landsat 8 LaSRC SR values.

The mean reflectance difference (MRD) is the mean of the difference between the reflectances of a SAAC-Net pixel and a Landsat 8 LaSRC pixel, which are in identical spectra and locations. This is computed in Equations 9. MRD attenuates reflectance due to the atmosphere, which can be used to correct the SAAC-Net SR. Overall, it is a simple and robust AC metric that can be combined with other metrics and applied across sensors.

$$MRD(\Delta\overline{\rho_\lambda}) = \overline{\rho}_\lambda^{SAAC-Net} - \overline{\rho}_\lambda^{LaSRC} \tag{9}$$

where, $\Delta\overline{\rho_\lambda}$ is the MRD between model predicted SR values and Landsat8 LaSRC SR values; $\overline{\rho}_\lambda^{SAAC-Net}$ and $\overline{\rho}_\lambda^{LaSRC}$ is the mean of SAAC-Net predicted and Landsat 8 LaSRC reflectance values of band λ, respectively, as calculated in Equation 10.

$$\overline{\rho}_\lambda = \frac{\sum_{i=1}^{n_\lambda} \rho_{i,\lambda}}{n_\lambda} \tag{10}$$

where, n_λ is the number of pixels in band λ. $\rho_{i,\lambda}$ is the reflectance value in the band λ and pixel i.

We also used the structural similarity index (SSIM) and correlation coefficient (r) to measure the reliability of the SAAC-Net image. SSIM is a perceptual measure that uses colour, texture, intensity, and structural information to assess AC accurately. It matches the structure, luminance, and contrast between the SAAC-Net BOA and the reference BOA image and evaluates SAAC-Net's ability to preserve the features of the scene. The correlation coefficient measures the linear relationship between the reflectance values of pixels of SAAC-Net and reference images to assess their similarity. It indicates the spatial consistency of the proposed method across the SAAC-Net image.

3.3. Model evaluation with Landsat 8 test data

The model's performance (with 8RB) was evaluated using RMSE, MRD, SSIM, and r for the Landsat 8 test dataset (cf. Table 2). Quantitative results for LCs are given in Table 4, and the qualitative results are shown in Figure 6. As per Table 4, the positive MRD value for all LCs suggests that the model predictions are overestimated compared to the Landsat 8 LaSRC SR values. This could potentially be attributed to the SAAC-Net's assumptions of lower scattering and absorption compared to the actual atmospheric conditions.

Table 4. Performance of SAAC-Net on Landsat 8 test data for bias, structural similarity, and coherence. All images are of months March, April, and May (Summer season) and November, December, and January (Winter season) of years 2019 and 2020.

Land cover Types	Landsat Rowpath	RMSE	MRD	SSIM	r
Urban Land	148044	0.051	0.005	0.96	0.99
Crop Land	148039	0.032	0.002	0.99	0.99
Deciduous Forest	135044	0.023	0.002	0.99	0.99
Evergreen Forest	135043	0.024	0.002	0.99	0.99
Fallow Land	149041	0.063	0.005	0.96	0.98
Waste Land	150043	0.059	0.006	0.96	0.98

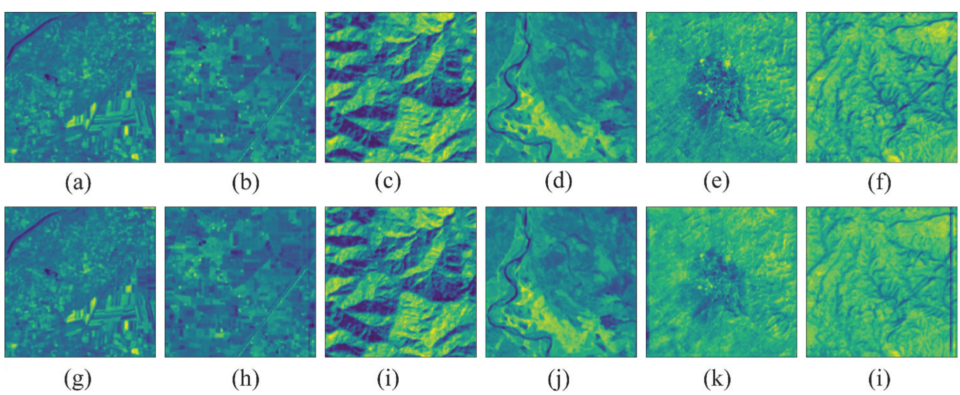

Figure 6. Results of various LCs. The first row shows the Landsat 8 BOA images (a - f), and the second row shows SAAC-Net-estimated images (g - l) for the following LC in order from left to right - Urban land, cropland, Deciduous Forest, Evergreen Forest, Fallow land, and wasteland with RMSE – 0.043, 0.030, 0.025, 0.023, 0.055, 0.053 respectively.

Notably, urban land, fallow land, and wasteland exhibit higher RMSE values when compared to other LC types. The higher RMSE in urban land is due to its heterogeneous structure with different reflectance properties and a higher degree of scattering and absorption due to pollutants, shadows, and specular reflections from urban facilities. The DL method will need an ancillary data source to account for these factors. Fallow land and wasteland are homogeneous but brighter than other areas, causing higher RMSE. It was observed that the average TOA reflectance of these areas was about 1.5 times more compared to other LCs. The mean TOA reflectance of wasteland and fallow land is 0.23, while for urban land, cropland, deciduous forest, and evergreen forest, it is 0.16, 0.17, 0.12, and 0.11, respectively. The other reason for the higher RMSE for fallow and wasteland is that atmospheric interference varies over space and time. The subtle difference in LC composition is challenging to detect and affects the accuracy of the AC. The other LCs, namely, cropland, deciduous, and evergreen forests, show lower MRD and RMSE values due to their homogeneous land cover, distinctive spectral properties, reduced variations in reflectance values due to homogeneity, and lower atmospheric interference.

The model exhibits high SSIM, suggesting that the structure of the Landsat BOA image and the model-predicted image are very similar. A high *r* points out that model-predicted images correlate well with the Landsat BOA images, and SAAC-Net has maintained spatial consistency across BOA images. Combining the results of Table 4 and Figure 6, one can observe the fidelity of the SAAC-Net in emulating the Landsat 8 values.

The scatter plot between SAAC-Net predictions and Landsat 8 LaSRC SR values for the blue band of one patch from the test location of the evergreen forest (Landsat ID 135043) is shown in Figure 7. The plot suggests a strong coherence between the model's prediction and Landsat 8 LaSRC SR. The 1:1 line is shown for visual comparison, and we can

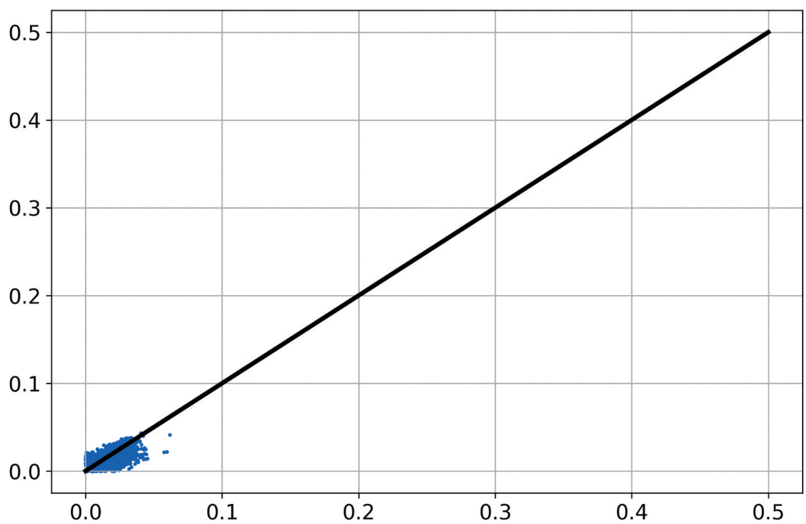

Figure 7. Scatter plot of blue band of one image patch of location 135043 Evergreen forest of date 01.04.2020. The X-axis represents SAAC-Net predicted SR values; the Y-axis represents Landsat 8 LaSRC SR values. $r = 0.96$, line fit: $0.003 \times x + 0.99$.

Table 5. Band-wise performance metrics of SAAC-Net on Landsat 8 LaSRC data. All images are of months March, April, and May (Summer season) and November, December, and January (Winter season) of years 2019 and 2020.

Land-cover Types Landsat Rowpath	Metric	Blue	Green	Red	NIR	SWIR1	SWIR2	All Bands
Urban Land - 148044	RMSE	0.071	0.049	0.042	0.050	0.048	0.042	0.051
	MRD	−0.03	0.00	0.00	0.00	0.01	0.02	0.005
	SSIM	0.84	0.88	0.86	0.86	0.88	0.90	0.96
	r	0.96	0.98	0.98	0.97	0.98	0.99	0.99
Crop Land - 148039	RMSE	0.014	0.019	0.022	0.041	0.044	0.037	0.032
	MRD	0.00	0.00	0.00	0.00	0.00	0.00	0.002
	SSIM	0.97	0.96	0.96	0.93	0.93	0.95	0.99
	r	0.91	0.90	0.92	0.86	0.89	0.93	0.99
Deciduous Forest - 135044	RMSE	0.011	0.012	0.013	0.041	0.029	0.019	0.023
	MRD	0.00	0.00	0.00	0.00	0.00	0.00	0.002
	SSIM	0.96	0.97	0.96	0.93	0.95	0.97	0.99
	r	0.96	0.96	0.96	0.93	0.94	0.95	0.99
Evergreen Forest - 135043	RMSE	0.011	0.012	0.011	0.043	0.029	0.018	0.024
	MRD	0.00	0.00	0.00	0.00	0.00	0.00	0.002
	SSIM	0.95	0.97	0.97	0.93	0.95	0.96	0.99
	r	0.97	0.97	0.98	0.92	0.93	0.96	0.99
Fallow Land - 149041	RMSE	0.088	0.052	0.052	0.064	0.058	0.055	0.063
	MRD	−0.05	0.00	0.00	0.00	0.01	0.02	0.005
	SSIM	0.86	0.92	0.91	0.88	0.91	0.91	0.96
	r	0.95	0.97	0.97	0.96	0.97	0.98	0.98
Waste Land - 150043	RMSE	0.079	0.047	0.045	0.057	0.056	0.055	0.059
	MRD	−0.04	0.00	0.00	0.00	0.01	0.02	0.006
	SSIM	0.86	0.91	0.90	0.88	0.91	0.90	0.96
	r	0.96	0.98	0.98	0.97	0.97	0.98	0.98

observe over and under-estimated model values, but overall, it maintains an excellent correlation with the reference SR values.

Band-wise values of all metrics are shown in Table 5. It is seen that the RMSE values for the blue band are the highest in urban land, fallow land, and wasteland as compared to the other bands, which is because the blue band has a shorter wavelength and is most sensitive to atmospheric interference. The blue band is sensitive to minor variations in soil or vegetation. These variations are difficult to correct, leading to higher RMSE. The low MRD values across bands indicate that the model bias is absent or very small. Overall, the model predicts well across all bands and LCs.

Apart from good prediction accuracy, the SAAC-Net takes less time to infer. It takes 0.10 sec on CPU to infer from the patch of size 128×128 pixel and 0.02 sec on GPU. These are faster than the physics-based model timings reported in (Prankur et al. 2021). Hence, the SAAC-Net balances the trade-off between prediction accuracy, computational complexity, and time.

3.4. Model generalization: evaluation over different LC and geographic location

The SAAC-Net model is trained on six LCs, as described in Section 2.1. To validate the effectiveness and generalization capability of the model, it is essential to evaluate model performance on LCs on which it has not been trained. Therefore, we tested it on plantation and shrubland LCs in India. The location chosen for the study is Kerala state, India (Latitude: 10.1632, Longitude: 76.6413) and Ratlam city

Table 6. SAAC-NET generalization over different LC and geographic location.

Location	LC Types	Date	Season	RMSE	MRD	SSIM	r
Kerala, India	Plantations	29.10.2021	Winter	0.051	0.034	0.88	0.90
		02.03.2021	Summer	0.045	0.030	0.79	0.88
Bikaner, India	Shrubland	31.12.2022	Winter	0.045	0.030	0.80	0.89
		11.04.2022	Summer	0.050	0.031	0.77	0.83
Arizona, U.S.A.	Urban Land,	27.01.2022	Winter	0.038	0.024	0.83	0.87
	Crop Land,	17.04.2022	Spring	0.039	0.024	0.82	0.88
	Waste Land	22.07.2022	Summer	0.042	0.026	0.79	0.87
		10.10.2022	Fall	0.044	0.025	0.82	0.92
Dubai, UAE	Urban Land,	09.12.2022	Winter	0.067	0.037	0.80	0.94
	Waste Land	04.09.2022	Spring	0.068	0.040	0.75	0.93

of Madhya Pradesh State, India (Latitude: 23.3315, Longitude: 75.0367). The results for plantation and shrubland LCs are shown in Table 6. The RMSE for both LCs is near the average RMSE of the SAAC-Net model for all locations shown in Table 4, which is 0.042. This shows that the model performs well for other LCs than the ones it is trained on.

It is crucial to see how the model behaves for images captured from different parts of the world with different seasons. We tested the SAAC-Net model with locations such as Arizona, U.S.A. (Latitude: 34.0489, Longitude: −111.0937) and Dubai, UAE (Latitude: 23.4241, Longitude: 53.8478). Arizona state observes four different seasons: Winter (Dec.–Feb.), Spring (Mar.–May), Summer (Jun.–Aug.), and Fall (Sep.–Nov.), with mean and max temperatures of 8°C to 40°C. Dubai observes mainly two seasons, Summer and Winter, with 16°C minimum to 50°C maximum temperature. The major LC types in Arizona are Urban Land, Crop Land, and Waste Land, whereas Waste Land and Urban Land are major LC types in Dubai.

The results for each evaluation metric for the U.S.A. and UAE are shown in Table 6. The RMSE of Arizona state is near the average RMSE of the SAAC-Net model, which is 0.042. However, the RMSE for Dubai is a little higher than the average RMSE of the model. This is because the average reflectance of this region is very high; it is nearly 0.27. This is similar to the high RMSE results we obtained for Fallow Land and Waste Land – which are high reflectance LCs, as shown in Table 4 This experiment proves the model's generalization capability for geographic locations with more extreme seasons than the training dataset.

We also interpret generalizations through heatmaps as they provide a visually intuitive representation of spatial data distributions and illustrate spatial variability by colour-coding data intensity across a geographic area (Shaito and Elmasri 2021). The heatmaps for SR help understand the variation in reflectance values across landscapes and enhance SR estimation by revealing data patterns. Figure 8 provides a visual representation in the form of heatmaps of SR for the above LCs across various spectral bands. These heatmaps illustrate a distinct pattern, with high reflectance values over Dubai's desert land LC compared to other LCs. Additionally, the heatmaps reveal a uniform trend in the blue spectral band, where reflectance values for all locations are near zero. These observations offer valuable insights into the spectral characteristics and reflective behaviours associated with the different LCs across different bands.

We also show in Section 4.4 that the RMSE of the model trained only with two LCs is not significantly different from the model trained using six LCs. Thus, the above experiments show that the model generalized well for different LCs, seasons, geographic locations, and datasets.

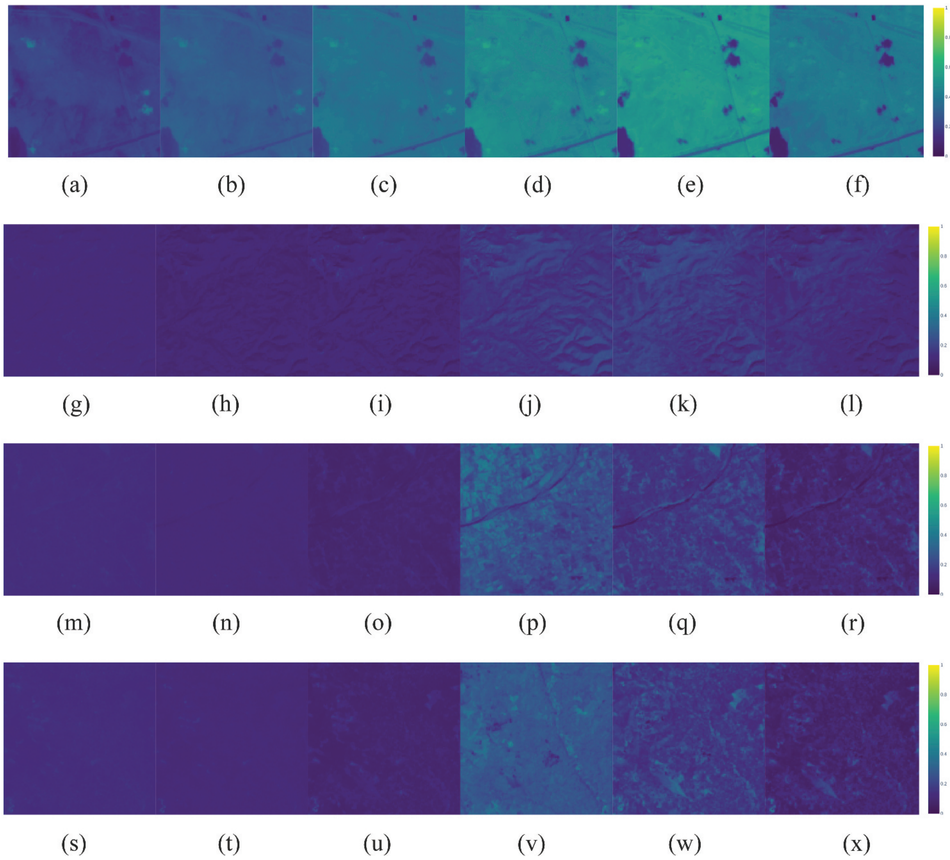

Figure 8. Heatmap of predicted SR values for Dubai(First row), Arizona, U.S.A. (second row), shrubland (Third row) and plantation (Fourth row) for bands Blue, Green, Red, NIR, SWIR1 and SWIR2 (left to right).

Table 7. Performance of SAAC-Net when compared with RadCalNet data.

Site	RMSE	MRD	SSIM	*r*
RailRoad	0.096	0.092	0.88	0.86
La Crau	0.025	0.021	0.93	0.90
Gobabeb	0.039	0.021	0.91	0.88

Table 8. Band-wise RMSE for RadCalNet locations.

Site	Blue	Green	Red	NIR	SWIR1	SWIR2
RailRoad	0.093	0.089	0.080	0.112	0.109	0.089
La Crau	0.042	0.029	0.028	0.063	0.043	0.044
Gobabeb	0.031	0.031	0.046	0.052	0.064	0.051

3.5. Model generalization: evaluation with RadCalNet data

As described in Section 2.1.2, RadCalNet provides in-situ measurements of SR values. We use the MRD, RMSE, SSIM, and *r* between the SAAC-Net predicted SR and RadCalNet measurements to check the model's performance. The result for each metric and RadCalNet location is shown in Table 7, and band-wise RMSE values are shown in Table 8.

It is essential to note that the geographical locations used for RadCalNet data differ from the SAAC-Net training data, with the latter originating from India. At the same time, RadCalNet encompasses locations in the U.S.A., France, and Namibia. Despite this disparity, the model exhibits low RMSE and high correlation coefficient values, signifying robust generalization capabilities and the potential to deliver accurate results across diverse global locations. RadCalNet locations yield higher MRD values and lower *r* values than the Landsat test locations (cf. Table 4). It could be due to the smaller geographical area of RadCalNet measurements over 1 km$\times$1 km or 90 m$\times$90 m. The RMSE values of the railroad location are higher than the other two locations, as the Railroad is a semi-arid region with sparse vegetation and is characterized by hills and valleys, which is a very different terrain from the training dataset location.

3.6. Comparison of SAAC-Net performance with other models

The SAAC-Net, at best, can match the performance of the Landsat 8 physics-based LaSRC model, as the training data is derived from it. To study the performance of SAAC-Net vis-a-vis Landsat 8 LaSRC, we used RadCalNet SR values as ground truth. Taking five data points from each location of RadCalNet from the year 2021, we computed RMSE, MRD, and *r* between SR values of RadCalNet with SAAC-Net predicted values and Landsat 8 LaSRC values. The results are shown in Table 9. As expected, the results show that the RMSE between the SAAC-Net-RadCalNet pair is higher than the RMSE between Landsat 8 LaSRC-RadCalNet pair. However, the increase is nominal for La Crau and Gobabeb, considering that SAAC-Net learns only using TOA and does not use any atmospheric parameters.

Figure 9 shows the band-wise SR spectra of SAAC-Net, RadCalNet, and Landsat 8 LaSRC at three RadCalNet locations. Both SAAC-Net and Landsat 8 LaSRC overestimate values for railroad location at all bands except Blue. However, SAAC-Net has better estimates for Green, Red, NIR, and SW1 bands. For LaCrau, Landsat 8 LaSRC is a better estimator, as SAAC-Net underestimates all bands except blue. The landscape is semi-arid, with agricultural land, grassland, shrubland, and rocky outcrops. The Gobabeb, a desert terrain, has Landsat 8 LaSRC overestimating at all bands, and SAAC-Net estimates are well matched for NIR, SW1, and SW2 bands.

Table 9. Relative performance comparison of SAAC-Net and LaSRC with RadCalNet. Subscript 1 indicates a pair (SAAC-Net, RadCalNet), and subscript 2 indicates a pair (Landsat 8 LaSRC, RadCalNet).

RadCalNet Sites	$RMSE_1$	$RMSE_2$	MRD_1	MRD_2	r_1	r_2
RailRoad	0.037	0.021	0.030	0.017	0.87	0.90
LaCrau	0.024	0.022	0.016	0.017	0.82	0.86
Gobabeb	0.015	0.012	0.014	0.009	0.98	0.99

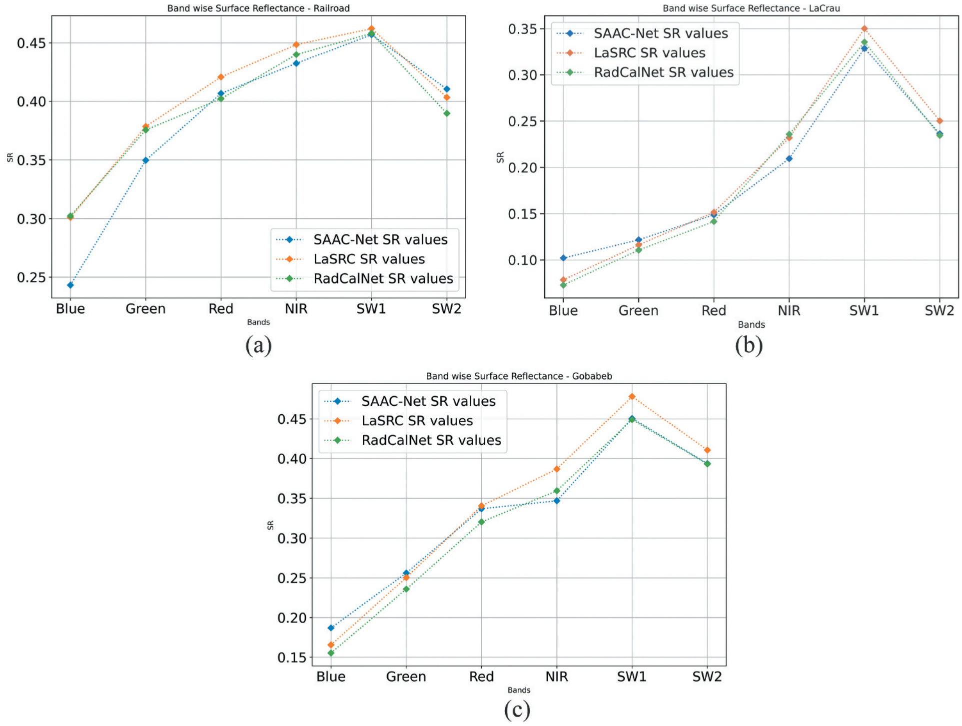

Figure 9. Band-wise SR spectra of SAAC-Net, RadCalNet, and Landsat 8 LaSRC. The X-axis represents wavelength, and the Y-axis represents reflectance. (a) railroad, (b) LaCrau, and (c) Gobabeb.

Table 10. Qualitative comparison of the proposed approach with other end-to-end DL-based method (Duffy et al. 2022).

Parameters	Deep Learning Framework – Paper	Our Proposed Approach
Architecture	Bayesian deep neural network	CNN with Residual blocks
Physics-based model	MAIAC	LASRC
Dataset	Himawari-8	Landsat-8
Spectrum	Hyperspectral	Multispectral
Seasonal parameter	No, but the seasonal analysis is done	Yes
Sensitivity analysis	Missing	Present
Qualitative results	Missing	Present
Bands	Red, Green, Blue, NIR, SWIR1, SWIR2	Red, Green, Blue, NIR, SWIR1, SWIR2

Overall, it can be observed that the SAAC-Net SR spectra follow trends and are in good agreement with the RadCalNet SR spectra at all the bands.

Very few researchers have used an end-to-end DL model to perform AC. One such approach implements MAIAC emulator (Duffy et al. 2022). The authors have designed a DL-based emulator of the MAIAC model using hyperspectral images provided by the Advanced Himawari Imager (AHI) sensor of the Himawari-8 satellite. It is difficult to compare quantitatively due to differences in the dataset and satellite used in both studies. Hence, we present a qualitative comparison with another DL-based approach for AC (Duffy et al. 2022) in Table 10.

Table 11. Impact of the season on RMSE. V = Variant. V1: 8 RB model with synthetic season band. V2: 8 RB model without synthetic season band. V3: GFEM without the 1×1 convolution block, and V4: Without GFEM. Note: The number with each LC denotes Landsat rowpath.

Land-cover Types	V1	V2	V3	V4
Urban Land – 148044	**0.051**	0.057	0.073	0.269
Crop Land – 148039	**0.032**	0.037	0.028	0.175
Deciduous Forest – 135043	**0.023**	0.027	0.022	0.144
Evergreen Forest – 135043	**0.024**	0.027	0.022	0.144
Fallow Land – 149041	**0.063**	0.066	0.093	0.319
Waste Land – 150043	**0.059**	0.060	0.097	0.319

4. Sensitivity study

We perform a sensitivity study to understand the importance of the season, RBs, skip connections, and dataset size.

4.1. Impact of season

As described earlier, seasons are one of the vital parameters as AOD and CWV significantly change with seasons. Hence, we have added an extra synthetic season band to guide the DL model. To validate the significance of this synthetic season band, we conducted experiments with the SAAC-Net model (eight Residual Blocks) under two scenarios: one with the season band (**V1**) and one without it (**V2**), utilizing the Landsat 8 test dataset. Table 11 shows that the RMSE of the model without the season band (V2) increases considerably for all LCs, which justifies the importance of feeding season information to the model while estimating SR values.

4.2. Impact of GFEM

A model with eight RBs was trained with the following variations to validate the need for the GFEM. The following notations have been used: V1: Original GFEM; V3: GFEM without the 1×1 convolution block; and V4: Without GFEM.

The result of this experiment is shown in Table 11. It is clear that the model V1 exhibits the lowest RMSE for every LC, and model V4 has the highest RMSE. This is because the local path loses the spatial characteristics of the image, and hence, the GFEM is necessary. Images shown in Figure 10 support the claim of using GFEM. It is visible that the images predicted from the model with V1 are very similar $RMSE\sim0.009$, $SSIM\sim0.99$, $r\sim0.99$ to Landsat 8 BOA images. Images predicted by V3 have a poor performance - $RMSE\sim0.014$, $SSIM\sim0.99$, $r\sim0.18$. Images predicted by the model without GFEM lose all spatial information from the original image and have the poorest performance metrics. Thus, we establish the efficacy of the GFEM block.

4.3. Number of residual blocks

We train the SAAC-Net using six LCs and study the model's performance with 8, 16, and 32 RBs. Table 12 shows that the model with eight RBs performs better than the other two models. It can be because 16/32 RBs increase the depth to capture complex features, but

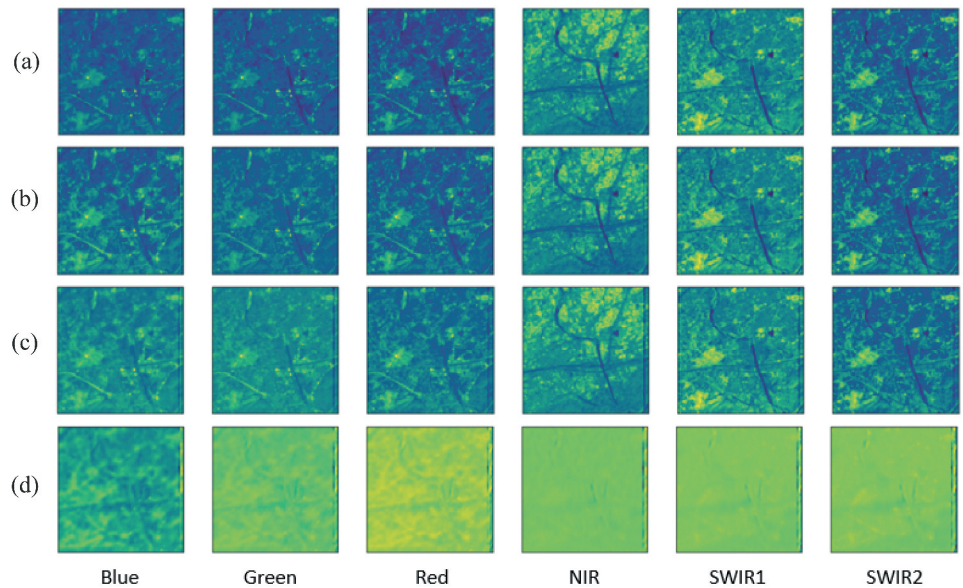

Figure 10. Impact of GFEM on band-wise generated images of 128×128 pixels size of LC urban land – 148044. (a) Landsat 8 BOA images, (b) predicted images: V1 - original GFEM (*RMSE* ~ 0.009, *SSIM* ~ 0.99, *r* ~ 0.99), (c) predicted images: V3 - GFEM without 1×1 convolution block (*RMSE* ~ 0.014, *SSIM* ~ 0.99, *r* ~ 0.18), (d) predicted images: V4 - without GFEM (*RMSE* ~ 0.23, *SSIM* ~ 0.65, *r* ~ 0.10).

they struggle to capture the diversity of the features for various LCs. Achieving a delicate balance between the model's depth (number of layers) and width (number of filters) within SAAC-Net is pivotal for optimal performance. While RBs alleviate the vanishing gradient problem, the gradient can still become very small as they propagate through the deeper layers. This can result in no significant performance gain with 16/32 RB models, as we observe that for a model with 8RBs and 32RBs, the average RMSE across all LCs is 0.042.

Moreover, no model results in the lowest RMSE for all six LCs. The RMSE values of cropland, deciduous, and evergreen forests are low compared to other LCs, irrespective of the number of RBs. This is because these LCs exhibit very low variability in the data. Also, adding RBs (e.g. 32) increases the number of parameters (e.g. 9.6 M parameters), and the

Table 12. RMSE performance of SAAC-Net trained on six LCs (Full data) and two LCs (Limited data) with 8/16/32 residual blocks. MP: Million parameters. Note: The number with each LC denotes Landsat rowpath.

	8 RB (2.5 MP)		16 RB (4.8 MP)		32 RB (9.6 MP)	
LC Types	Full Data	Limited Data	Full Data	Limited Data	Full Data	Limited Data
Urban Land – 148044	0.051	0.066	0.053	0.063	0.055	0.064
Crop Land – 148039	0.032	0.035	0.032	0.034	0.031	0.035
Deciduous Forest – 135044	0.023	0.023	0.024	0.025	0.025	0.025
Evergreen forest – 135043	0.024	0.025	0.025	0.025	0.025	0.026
Fallow Land – 149041	0.063	0.076	0.059	0.070	0.063	0.072
Waste Land – 150043	0.059	0.073	0.059	0.067	0.057	0.068

model complexity increases without significant performance improvement. Hence, in this paper, we selected the eight RB SAAC-Net model for experiments in the paper.

4.4. Model performance on limited dataset

Training a model with an extensive dataset involves heavy computational resources and time. Moreover, there are cases where TOA images of different LC types are unavailable for some sensors. Hence, testing the model's effectiveness trained on limited data is crucial. In one such experiment, we trained the model using only two LCs – urban land and cropland. The reasons for choosing these two LCs are as follows: urban land has more variation than any other LC type, and cropland covers a maximum part of the Indian subcontinent. The training was done using 6400 patches of these two LCs and testing on 4800 patches of all LCs.

Table 12 also shows the RMSE values of different LC types with limited data. The results show that the RMSE of the 8/16/32 RB model trained with 2-LC increases for urban land, cropland, evergreen forest, fallow land, and wasteland. One can easily relate the interplay between accuracy and time complexity. Training with all 6-LCs increases the model's accuracy as one observes lower RMSE. However, a higher accuracy will also increase the training time for the model by approximately three times, as found during our experiments.

This experiment also tests the model's generalization capability, i.e. how it performs for an unseen LC. One can observe from Table 12 that the model generalizes well, as RMSE for a model trained with two LCs is not drastically different from RMSE results for a model trained with six LCs.

5. Conclusion and future work

This paper proposes SAAC-Net, an end-to-end season-aware DNN, to predict SR from TOA images. The designed and trained model is used to predict SR values without using information about atmospheric parameters such as AOD, water vapour, and air pressure. The predicted SR of the SAAC-Net has been assessed with the Landsat 8 LaSRC physics-based model and on-site measurements provided by RadCalNet. Results have shown the potential and effectiveness of the DNN-based approach in performing AC.

Although training of the model is compute-intensive, testing SAAC-Net to the given image requires a very low computational load, making the model suitable for real-time applications. For instance, it takes about 0.10 s for our model with eight RBs to perform AC on input images of size 128×128 pixels on a CPU and 0.02 on a GPU.

The SAAC-Net model was trained using TOA and BOA image pairs generated by the Landsat 8 LaSRC algorithm, which relies on a physics-based model. While theoretically robust, such physics-based systems often entail significant computational costs and necessitate numerous assumptions and simplifications. Notably, the physics-based model exhibits an error rate of approximately 10–15% (Badawi et al. 2019) in estimating SR due to inherent approximations in estimating various atmospheric parameters and the underlying assumptions of RTM. Consequently, the performance of the SAAC-Net model is inherently tethered to the limitations of the physics-based model upon which it is trained. In an ideal research scenario, our training dataset would encompass a comprehensive array of BOA measurements derived through on-site photospectrometry conducted across a broad and diverse geographical area. This would serve as a benchmark dataset for training the DL model for AC, minimizing the influences of the physics-based model's limitations. However, in practice, the acquisition of such a dataset is a challenging task. Conducting on-site photospectrometry to cover diverse geographic regions spanning varying environmental conditions and diverse landscapes is a resource-intensive task that demands both time and substantial financial investments.

While addressing seasonal and spatial variability, this study does not account for the temporal variability that occurs over extended timeframes, potentially reducing the model's effectiveness when applied to imagery obtained decades later, primarily due to the evolving atmospheric conditions and alterations in aerosol density over time (Singh et al. 2022). Such temporal discrepancies introduce a dataset shift problem (Shah et al. 2023), potentially compromising the model performance. This requires a more comprehensive DL model that accounts for spatial and seasonal variations and temporal changes. We plan to study the temporal evolution and design a spatially, seasonally, and temporally aware DL model for performing accurate AC.

Acknowledgment

The authors thank the School of Engineering and Applied Science, Ahmedabad University, and L D College of Engineering for providing the infrastructural support. The authors also thank SIPG group members at SAC ISRO, Ahmedabad, for their insightful comments.

Disclosure statement

No potential conflict of interest was reported by the author(s).

Funding

Part of this work is carried out on the GPU purchased under Grant by the Department of Science and Technology-Gujarat Council of Science and Technology (DST-GUJCOST) under Grant GUJCOST/STI/2021-22/3858.

ORCID

Maitrik Shah http://orcid.org/0000-0002-4856-9867
Mehul S Raval http://orcid.org/0000-0002-3895-1448
Debajyoti Dhar http://orcid.org/0000-0002-3547-4391

References

Acharya, P., and S. Sreekesh. 2013. "Seasonal Variability in Aerosol Optical Depth Over India: A Spatio-Temporal Analysis Using the MODIS Aerosol Product." *International Journal of Remote Sensing* 34 (13): 4832–4849. https://doi.org/10.1080/01431161.2013.782114.

Acito, N., and M. Diani. 2018. “Atmospheric Column Water Vapor Retrieval from Hyperspectral VNIR Data Based on Low-Rank Subspace Projection.” *IEEE Transactions on Geoscience and Remote Sensing* 56 (7): 3924–3940. https://doi.org/10.1109/TGRS.2018.2816593.

Acito, N., M. Diani, and G. Corsini. 2020. “CWV-Net: A Deep Neural Network for Atmospheric Column Water Vapor Retrieval from Hyperspectral Vnir Data.” *IEEE Transactions on Geoscience and Remote Sensing* 58 (11): 8163–8175. https://doi.org/10.1109/TGRS.2020.2987905.

Anderson, G. P., G. W. Felde, M. L. Hoke, A. J. Ratkowski, T. W. Cooley, J. H. Chetwynd, J. A. Gardner, et al. 2002. “MODTRAN4-Based Atmospheric Correction Algorithm: FLAASH (Fast Line-Of-Sight Atmospheric Analysis of Spectral Hypercubes).” In *Algorithms and Technologies for Multispectral, Hyperspectral, and Ultraspectral Imagery VIII*, edited by S. S. Sylvia and E. L. Paul, Vol. 4725, 65–71. International Society for Optics and Photonics, SPIE. https://doi.org/10.1117/12.478737

Angelopoulou, T., N. Tziolas, A. Balafoutis, G. Zalidis, and D. Bochtis. 2019. “Remote Sensing Techniques for Soil Organic Carbon Estimation: A Review.” *Remote Sensing* 11 (6): 676. https://doi.org/10.3390/rs11060676.

Badawi, M., D. Helder, L. Leigh, and X. Jing. 2019. “Methods for Earth-Observing Satellite Surface Reflectance Validation.” *Remote Sensing* 11 (13): 1543. https://www.mdpi.com/2072-4292/11/13/1543.

Bouvet, M., K. J. Thome, B. Berthelot, A. Bialek, J. S. Czapla-Myers, N. P. Fox, P. Goryl, et al. 2019. “RadCalnet: A Radiometric Calibration Network for Earth Observing Imagers Operating in the Visible to Shortwave Infrared Spectral Range.” *Remote Sensing* 11 (20): 2401. https://doi.org/10.3390/rs11202401.

Chavez, P. S. 1988. “An Improved Dark-Object Subtraction Technique for Atmospheric Scattering Correction of Multispectral Data.” *Remote Sensing of Environment* 24 (3): 459–479. https://doi.org/10.1016/0034-4257(88)90019-3.

Chen, J. M. 2021. “Carbon neutrality: Toward a sustainable future.” *The Innovation* 2 (3): 100127. https://doi.org/10.1016/j.xinn.2021.100127.

Chen, Y., H. Jiang, L. Chunyang, X. Jia, and P. Ghamisi. 2016. “Deep Feature Extraction and Classification of Hyperspectral Images Based on Convolutional Neural Networks.” *IEEE Transactions on Geoscience and Remote Sensing* 54 (10): 6232–6251. https://doi.org/10.1109/TGRS.2016.2584107.

DIOUF, D., A. Niang, and S. Thiria. 2019. “Deep Learning Based Multiple Regression to Predict Total Column Water Vapor (Tcwv) from Physical Parameters in West Africa by Using Keras Library.” *International Journal of Data Mining & Knowledge Management Process* 9 (6): 13–21. https://doi.org/10.5121/ijdkp.2019.9602.

Division, P. 2020. *India 2020: Reference Annual Book*. Publications Division Ministry of Information & Broadcasting. https://books.google.co.in/books?id=yOfQDwAAQBAJ.

Duffy, K., T. J. Vandal, W. Wang, R. R. Nemani, and A. R. Ganguly. 2022. “A Framework for Deep Learning Emulation of Numerical Models with a Case Study in Satellite Remote Sensing.” *IEEE Transactions on Neural Networks and Learning Systems*, 1–12.

Fadaeddini, A., M. Eshghi, and B. Majidi. 2018. “A Deep Residual Neural Network for Low Altitude Remote Sensing Image Classification.” *6th Iranian Joint Congress on Fuzzy and Intelligent Systems*, Kerman, Iran, 43–46.

Gao, H., Z. Chen, and X. Feng. 2022. “Adaptive Spectral-Spatial Feature Fusion Network for Hyperspectral Image Classification Using Limited Training Samples.” *International Journal of Applied Earth Observation and Geoinformation* 107:102687. https://doi.org/10.1016/j.jag.2022.102687.

Holben, B. N., T. FêŽ¬ Eck, I. Al Slutsker, D. Tanré, J. P. Buis, A. Setzer, E. Vermote, et al. 1998. “AERONET—A Federated Instrument Network and Data Archive for Aerosol Characterization.” *Remote Sensing of Environment* 66 (1): 1–16. https://doi.org/10.1016/S0034-4257(98)00031-5.

Hsu, N. C., S.-C. Tsay, M. D. King, and J. R. Herman. 2006. “Deep Blue Retrievals of Asian Aerosol Properties During ACE-Asia.” *IEEE Transactions on Geoscience and Remote Sensing* 44 (11): 3180–3195. https://doi.org/10.1109/TGRS.2006.879540.

Jackson, J. M., H. Liu, I. Laszlo, S. Kondragunta, L. A. Remer, J. Huang, and H.-C. Huang. 2013. "Suomi-NPP VIIRS aerosol algorithms and data products." *Journal of Geophysical Research Atmospheres* 118 (22): ,12,673–12,689,. https://doi.org/10.1002/2013JD020449.

Kaiming, H., X. Zhang, S. Ren, and J. Sun. 2016. "Deep Residual Learning for Image Recognition." In *Proceedings of 2016 IEEE Conference on Computer Vision and Pattern Recognition*, CVPR 16, Jun, 770–778. IEEE. http://ieeexplore.ieee.org/document/7780459 .

Kaufman, Y. J., D. Tanré, L. Ao Remer, E. F. Vermote, A. Chu, and B. N. Holben. 1997. "Operational Remote Sensing of Tropospheric Aerosol Over Land from EOS Moderate Resolution Imaging Spectroradiometer (Paper 96JD03988)." *JOURNAL of GEOPHYSICAL RESEARCH-ALL SERIES-* 102 (D14): 17051–17067. https://doi.org/10.1029/96JD03988.

Kotchenova, S. Y., and E. F. Vermote. 2007. "Validation of a Vector Version of the 6S Radiative Transfer Code for Atmospheric Correction of Satellite Data. Part II. Homogeneous Lambertian and Anisotropic Surfaces." *Applied Optics* 46 (20): 4455–4464. https://doi.org/10.1364/AO.46.004455.

Litu, R., Y. Bhateja, A. Garg, I. Mishra, S. Manthira Moorthi, and D. Dhar. 2019. "DeepSwir: A Deep Learning Based Approach for the Synthesis of Short-Wave InfraRed Band Using Multi-Sensor Concurrent Datasets." http://arxiv.org/abs/1905.02749.

Liu, Q., and X. Liang. 2023. "Physics Constraint Deep Learning Based Radiative Transfer Model." *Optics Express* 31 (17): 28596–28610. https://doi.org/10.1364/OE.493818.

Lyapustin, A. I., Y. Wang, I. Laszlo, T. Hilker, F. G. Hall, P. J. Sellers, C. J. Tucker, and S. V. Korkin. 2012. "Multi-Angle Implementation of Atmospheric Correction for MODIS (MAIAC): 3. Atmospheric Correction." *Remote Sensing of Environment* 127:385–393. https://doi.org/10.1016/j.rse.2012.09.002.

Manil, M., R. Ramachandran, M. Ramasubramanian, I. Gurung, B. Freitag, A. Kaulfus, D. Bollinger, D. J. Cecil, and J. Miller. 2020. "Deepti: Deep-Learning-Based Tropical Cyclone Intensity Estimation System." *IEEE Journal of Selected Topics in Applied Earth Observations and Remote Sensing* 13:4271–4281. https://doi.org/10.1109/JSTARS.2020.3011907.

Patel, V. K., and J. Kuttippurath. 2022. "Significant Increase in Water Vapour Over India and Indian Ocean: Implications for Tropospheric Warming and Regional Climate Forcing." *Science of the Total Environment* 838:155885. https://doi.org/10.1016/j.scitotenv.2022.155885.

Peng, D., Y. Zhang, and H. Guan. 2019. "End-To-End Change Detection for High Resolution Satellite Images Using Improved UNet++." *Remote Sensing* 11 (11): 1382. https://doi.org/10.3390/rs11111382.

Prankur, R., Y. Bhateja, I. Misra, S. Manthira Moorthi, and D. Dhar. 2021. "An Efficient Machine Learning Approach for Atmospheric Correction." *The Journal of the Indian Society of Remote Sensing* 49 (10): 2539–2548. https://doi.org/10.1007/s12524-021-01406-6.

Richter, R., and D. Schläpfer. 2019. "Atmospheric and Topographic Correction (ATCOR Theoretical Background Document)" *DLR IB*. Wessling, Germany. https://www.rese-apps.com/software/atcor/manual-papers.html .

Roy, D. P., M. A. Wulder, T. R. Loveland, C. E. Woodcock, R. G. Allen, M. C. Anderson, D. Helder, et al. 2014. "Landsat-8: Science and Product Vision for Terrestrial Global Change Research." *Remote Sensing of Environment* 145:154–172. https://doi.org/10.1016/j.rse.2014.02.001.

Saeidi, V., S. Teymoor Seydi, B. Kalantar, N. Ueda, B. Tajfirooz, and F. Shabani. 2023. "Water Depth Estimation from Sentinel-2 Imagery Using Advanced Machine Learning Methods and Explainable Artificial Intelligence." *Geomatics, Natural Hazards and Risk* 14 (1): 2225691. https://doi.org/10.1080/19475705.2023.2225691.

Schläpfer, D., C. C. Borel, J. Keller, and K. I. Itten. 1998. "Atmospheric Precorrected Differential Absorption Technique to Retrieve Columnar Water Vapor." *Remote Sensing of Environment* 65 (3): 353–366. https://doi.org/10.1016/S0034-4257(98)00044-3.

Shah, M., M. S. Raval, S. Divakaran, and P. Patel. 2023. "Study and Impact Analysis of Data Shift in Deep Learning Based Atmospheric Correction." In *IGARSS 2023 - 2023 IEEE International Geoscience and Remote Sensing Symposium*, Pasadena, CA, USA.

Shaito, M., and R. Elmasri. 2021. "Map Visualization Using Spatial and Spatio-Temporal Data: Application to COVID-19 Data." In *Proceedings of the 14th PErvasive Technologies Related to Assistive Environments Conference*, PETRA '21, New York, NY, USA, 284–291. Association for Computing Machinery. https://doi.org/10.1145/3453892.3461336.

She, L., H. K. Zhang, Z. Bu, Y. Shi, L. Yang, and J. Zhao. 2022. "A Deep-Neural-Network-Based Aerosol Optical Depth (AOD) Retrieval from Landsat-8 Top of Atmosphere Data." *Remote Sensing* 14 (6): 1411. https://doi.org/10.3390/rs14061411.

She, L., H. K. Zhang, L. Zhengqiang, G. de Leeuw, and B. Huang. 2020. "Himawari-8 Aerosol Optical Depth (AOD) Retrieval Using a Deep Neural Network Trained Using AERONET Observations." *Remote Sensing* 12 (24): 4125. https://www.mdpi.com/2072-4292/12/24/4125.

Simonyan, K., A. Zisserman, and A. Zisserman. 2014. "Learning Local Feature Descriptors Using Convex Optimisation." *IEEE Transactions on Pattern Analysis & Machine Intelligence* 36 (8): 1573–1585. https://doi.org/10.1109/TPAMI.2014.2301163.

Singh, R., V. Singh, A. Sagar Gautam, S. Gautam, M. Sharma, P. Singh Soni, K. Singh, and A. Gautam. 2022. "Temporal and Spatial Variations of Satellite-Based Aerosol Optical Depths, Angstrom Exponent, Single Scattering Albedo, and Ultraviolet-Aerosol Index Over Five Polluted and Less-Polluted Cities of Northern India: Impact of Urbanization and Climate Change." *Aerosol Science and Engineering* 7 (1): 131–149. https://doi.org/10.1007/s41810-022-00168-z.

Smith, G. M., and E. J. Milton. 1999. "The Use of the Empirical Line Method to Calibrate Remotely Sensed Data to Reflectance." *International Journal of Remote Sensing* 13 (13): 2653–2662. https://doi.org/10.1080/014311699211994.

Smith, G. M., and E. J. Milton. 2012. "Quick Atmospheric Correction Code: Algorithm Description and Recent Upgrades." *Optical Engineering* 51 (11): 1–12. https://doi.org/10.1117/1.OE.51.11.111719.

Tarasiou, M., E. Chavez, and S. Zafeiriou. 2023. "ViTs for SITS: Vision Transformers for Satellite Image Time Series". *IEEE/CVF Conference on Computer Vision and Pattern Recognition (CVPR)*, Vancouver, BC, Canada, 10418–10428. https://doi.org/10.1109/CVPR52729.2023.01004.

Vermote, E., C. Justice, M. Claverie, and B. Franch. 2016. "Preliminary Analysis of the Performance of the Landsat 8/OLI Land Surface Reflectance Product." *Remote Sensing of Environment* 185:46–56. Landsat 8 Science Results. https://www.sciencedirect.com/science/article/pii/S0034425716301572 .

Vermote, E. F., D. Tanre, J. L. Deuze, M. Herman, and J.-J. Morcette. 1997. "Second Simulation of the Satellite Signal in the Solar Spectrum, 6S." *An Overview IEEE Transactions on Geoscience and Remote Sensing* 35 (3): 675–686. https://doi.org/10.1109/36.581987.

Yao, Y., X. Zhong, Y. Zheng, and Z. Wang. 2023. "A Physics-Incorporated Deep Learning Framework for Parameterization of Atmospheric Radiative Transfer." *Journal of Advances in Modeling Earth Systems* 15 (5): e2022MS003445. https://agupubs.onlinelibrary.wiley.com/doi/abs/10.1029/2022MS003445 .

Zhang, R., J. J. Qu, Y. Liu, X. Hao, C. Huang, and X. Zhan. 2015. "Detection of Burned Areas from Mega-Fires Using Daily and Historical MODIS Surface Reflectance." *International Journal of Remote Sensing* 36 (4): 1167–1187. https://doi.org/10.1080/01431161.2015.1007256.

Zhao, T., R. Chen, X. Jindong, and M. Xiangyue. 2021. "Remote Sensing Image Segmentation Based on the Fuzzy Deep Convolutional Neural Network." *International Journal of Remote Sensing* 42 (16): 6264–6283. https://doi.org/10.1080/01431161.2021.1938738.

Zhou, Q., S. Wang, N. Liu, P. A. Townsend, C. Jiang, B. Peng, W. Verhoef, and K. Guan. 2023. "Towards Operational Atmospheric Correction of Airborne Hyperspectral Imaging Spectroscopy: Algorithm Evaluation, Key Parameter Analysis, and Machine Learning Emulators." *ISPRS Journal of Photogrammetry and Remote Sensing* 196:386–401. https://doi.org/10.1016/j.isprsjprs.2022.11.016.